Geophys. J. Int. (2002) **149,** 338–348

Sensitivity distributions of different borehole electrode configurations considering a model with a cylindrical coaxial boundary

M. Furche and A. Weller

Institut für Geophysik, Technische Universität Clausthal, Arnold-Sommerfeld-Str. 1, D-38678 *Clausthal-Zellerfeld, Germany*
E-mail: andreas.weller@tu-clausthal.de

Accepted 2001 November 5. Received 2001 September 11; in original form 2000 November 30

SUMMARY

The sensitivity distributions of different electrode configurations are computed for both a homogeneous resistivity distribution and a model consisting of two vertical zones of homogeneous resistivity. The inner zone around the borehole axis represents a borehole filled with mud and the outer zone is the undisturbed formation. The sensitivity of the homogeneous model is independent of resistivity. Whereas the sensitivity in the case of the cylindrical coaxial boundary depends on the contrast between formation resistivity and mud resistivity. With increasing contrast, the sensitivity distribution changes dramatically for all investigated electrode configurations.

The sensitivity patterns are used to illustrate the ability of different electrode configurations to delineate thin layers. The superiority of focused tools in comparison to normal logs can clearly be shown if the effect of variable bucking currents is included.

Key words: borehole geophysics, electrical resistivity, numerical techniques.

1 INTRODUCTION

Multi-electrode resistivity tools yield a number of normal or lateral curves which can be used to simulate the response of a variety of conventional or focused tools. Synthetically focused logs resulting from multi-electrode measurements have proved that a good vertical resolution can be achieved without any technical focusing (Schön & Weller 1984). However, a single focused log does not use the full information provided by multi-electrode tools. Sophisticated inversion algorithms perform the transformation of the measured quantities into a reliable resistivity model (Fan 1998; Hakvoort *et al.* 1998). The tool design should consider the sensitivity distribution of the measured quantities which shows where the information comes from. The sensitivity describes the influence of a slight change of the conductivity in a small volume element on the measured apparent resistivity of a certain electrode configuration.

Several authors have published the sensitivity distribution of various surface configurations (e.g. Barker 1979; Kampke 1999). Different methods of calculating the sensitivity are given by Weller *et al.* (1996) and Spitzer (1998). The sensitivity distribution is not only used to characterize the resolution of the electrode configuration. The sensitivity matrix, which is also called the Jacobian matrix, relates changes of the resistivity model to changes in the measured data. Most inversion procedures that are performed iteratively are based on knowledge of the sensitivity matrix. Since the sensitivity depends on the resistivity model, the sensitivity matrix has to be updated with changes of the model. The use of the sensitivity of a homogeneous half-space can only be a rough approximation. Loke & Barker (1996) present a rapid least-squares inversion based on a quasi-Newton update of sensitivity. Seichter (1998) uses the fully updated sensitivity matrix in a simultaneous iterative reconstruction technique.

2 COMPUTING OF SENSITIVITY DISTRIBUTION

2.1 Definition of sensitivity

To compute the sensitivity distribution in the borehole environment the relevant volume Ω is divided into j elements Ω_j of resistivity ρ_j. Since the dependence of the azimuth angle is neglected, only two dimensions are considered: the vertical z-direction and the radial r-direction. Fig. 1 shows the scheme of the grid that is used for computing. The grid size is 100 elements in the r-direction and 200 elements in the z-direction. The problem is formulated in cylindrical coordinates. The sensitivity matrix

$$\mathbf{S} = \{s_{i,j}\}_{\substack{i=1,\ldots,M \\ j=1,\ldots,N}} \tag{1}$$

with the coefficients

$$s_{i,j} = \frac{\partial y_i}{\partial x_j} \tag{2}$$

can be formulated for different measured quantities y_i and model parameters x_j. Since the order of resistivities varies over several decades, a logarithmic presentation of the measured apparent resistivity $\hat{\rho}_i$ and the model resistivity ρ_j is an appropriate choice:

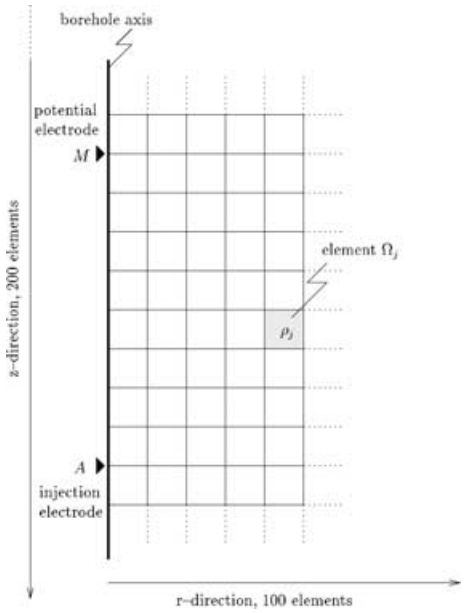

Figure 1. Scheme of the grid used to compute the sensitivity distribution.

$$y_i = \ln \hat{\rho}_i, \tag{3}$$

$$x_j = \ln \rho_j. \tag{4}$$

First, consider the case of the pole–pole configuration with the injection electrode A at the position described by the space vector $\mathbf{r}_A$ and the potential electrode M at the position $\mathbf{r}_M$. The sensitivity coefficients of the volume element Ω_j for the ith pole–pole configuration is (Weller *et al.* 1996)

$$s_{i,j} = \frac{K_i}{\hat{\rho}_i I^2 \rho_j} \int_{\Omega_j} \nabla V(\mathbf{r} \mid \mathbf{r}_A) \cdot \nabla V(\mathbf{r} \mid \mathbf{r}_M)\, d^3r, \tag{5}$$

where K_i is the geometric factor and $V(\mathbf{r} \mid \mathbf{r}_A)$ the potential at the location of vector $\mathbf{r}$ if the injection electrode is located at $\mathbf{r}_A$. The corresponding return electrodes B and N are assumed to be shifted to infinity. The equation is valid for any conductivity distribution. It implies that the gradient of the potential caused by a current injection at both positions A and M is needed to determine the sensitivity coefficients. The sensitivity distribution of any electrode configuration can be assembled by superimposing several involved pole–pole configurations. For example, the sensitivity coefficient of a four-electrode configuration with the current electrodes A and B and the potential electrodes M and N results in

$$s_{i,j} = \frac{K_i}{\hat{\rho}_i I^2 \rho_j} \{\hat{s}_{A,M} - \hat{s}_{A,N} - \hat{s}_{B,M} + \hat{s}_{B,N}\}, \tag{6}$$

using the abbreviation

$$\hat{s}_{A,M} = \int_{\Omega_j} \nabla V(\mathbf{r} \mid \mathbf{r}_A) \cdot \nabla V(\mathbf{r} \mid \mathbf{r}_M)\, d^3r, \tag{7}$$

where K_i is the corresponding four-electrode geometric factor.

2.2 Homogeneous space

In a homogeneous full space, each value of apparent resistivity $\hat{\rho}_i$ is equal to the constant resistivity of all elements $\rho_j = \rho$. The potential is given by the equation

$$V(\mathbf{r} \mid \mathbf{r}_A) = \frac{\rho I}{4\pi |\mathbf{r} - \mathbf{r}_A|}. \tag{8}$$

Considering (8), eq. (5) results in

$$s_{i,j} = \frac{K_i}{16\pi^2} \int_{\Omega_j} \nabla \frac{1}{|\mathbf{r} - \mathbf{r}_A|} \cdot \nabla \frac{1}{|\mathbf{r} - \mathbf{r}_M|}\, d^3r. \tag{9}$$

It can be seen that the sensitivity distribution is independent of the resistivity in a homogeneous space. The integration is approximated by the product of the cell volume and the two gradients in the middle of the cell:

$$s_{i,j} \cong \frac{K_i}{8\pi} r_j \Delta r_j \Delta z_j \times \frac{r_j^2 + (z_j - z_A)(z_j - z_M)}{\left[\sqrt{r_j^2 + (z_j - z_A)^2}\right]^3 \left[\sqrt{r_j^2 + (z_j - z_M)^2}\right]^3}, \tag{10}$$

where z_A and z_M are the z-coordinates of the electrodes A and M, respectively. The corresponding r-coordinates vanish because the electrodes are placed at the borehole axis.

2.3 Model with a cylindrical coaxial boundary

Since the average formation resistivity may be different from the mud resistivity, the homogeneous space model is too simple to calculate a reliable sensitivity distribution in practice. It is better to use a cylindrical coaxial boundary between a mud-filled borehole and the undisturbed formation. Fig. 2 shows the scheme of the model. In the centre is the borehole axis surrounded by the cylindrical space of the borehole with resistivity ρ_0 and diameter $d_0 = 2r_0$. Outside, there is the undisturbed formation with resistivity ρ_t. An electrode configuration is assumed with current injection along the axis. The potential function $V(r, z)$ is defined in cylindrical coordinates. Since we want to know the sensitivity in the formation, we require the potential $V(r, z)$ and its spatial derivatives for $r \geq r_0$, which are given by the following two equations:

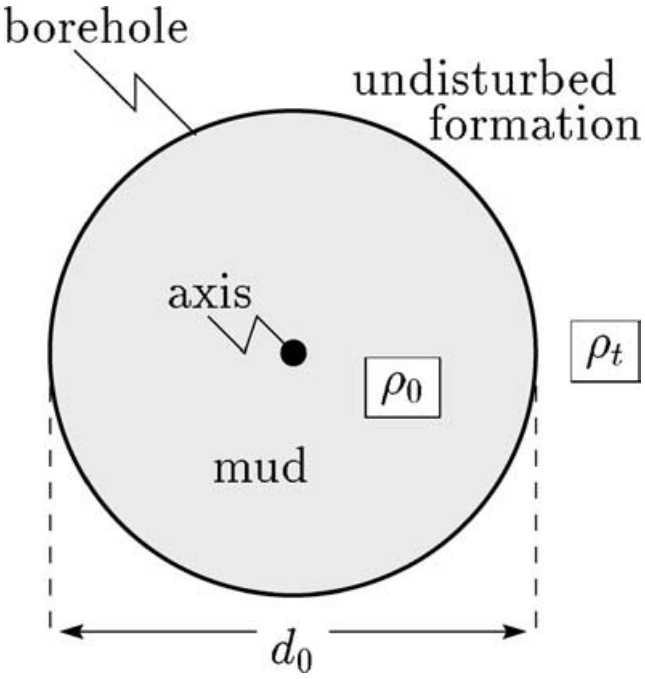

Figure 2. Scheme of a cylindrical coaxial model of a borehole filled with mud and an undisturbed formation outside.

$$\frac{\partial V(r,z)}{\partial r} = \frac{-\rho_t I}{2\pi^2 r_0^2} \times \int_0^\infty D_t(m) K_1(mr/r_0) m \cos(mz/r_0)\, dm, \quad \forall r \geq r_0 \tag{11}$$

and

$$\frac{\partial V(r,z)}{\partial z} = \frac{-\rho_t I}{2\pi^2 r_0^2} \times \int_0^\infty D_t(m) K_0(mr/r_0) m \sin(mz/r_0)\, dm, \quad \forall r \geq r_0 \tag{12}$$

with

$$D_t(m) = \frac{I_1(m)K_0(m) + I_0(m)K_1(m)}{(\rho_t/\rho_0) I_1(m)K_0(m) + I_0(m)K_1(m)}, \tag{13}$$

and I_0, K_0, I_1 and K_1 are the modified Bessel functions of order zero and one, respectively. The details of the mathematical origin of eqs (11)–(13) and the numerical calculation are explained in Appendix A. It can be concluded from eq. (13) that the sensitivity only depends on the resistivity ratio ρ_t/ρ_0 and not on the absolute values of ρ_0 and ρ_t.

Finally, eqs (11) and (12) are inserted in eq. (5) to calculate the sensitivity. Since ρ_t corresponds to ρ_j, a factor of $\rho_t/\hat{\rho}_i$ has to be considered. For a given resistivity contrast ρ_t/ρ_0, the apparent resistivity $\hat{\rho}_i$ is calculated by a numerical forward modelling.

3 COMPARISON OF SENSITIVITY IMAGES

The sensitivity images of four different configurations used in electrical logging are investigated. Since the sensitivity depends on the resistivity ratio ρ_t/ρ_0, four different values 0.1, 1.0, 10 and 100 are chosen to demonstrate their influence. The ratio 1.0 corresponds to the homogeneous space. The procedure described in Section 2.3 and Appendix A is used to calculate the sensitivity distribution for the other resistivity ratios. A grid size of 200 elements in the vertical direction and 100 elements in the radial direction is used (see Fig. 1). In the sensitivity images, the r- and z-coordinates are normalized to the borehole radius r_0. All elements of the grid are squares of side-length $0.1r_0$. Since the sensitivity distribution is only shown for the undisturbed formation, the borehole is presented as a grey bar on the left-hand side of each figure. The electrodes of each configuration are indicated by small triangles and the letters A, B, M_n, S_n, ..., on the left-hand margin.

Since the calculated sensitivity values vary over several decades they are transformed on a logarithmic scale using the formula $s'_{i,j} = \mathrm{sgn}(s_{i,j}) \log(|s_{i,j}| \times 10^6)$ and setting all sensitivities with an absolute value smaller than 10^{-6} to zero. This transformation preserves the sign of $s_{i,j}$ in $s'_{i,j}$. For a positive value of $s'_{i,j}$, a resistivity increase in an element Ω_j results in an increase of apparent resistivity $\hat{\rho}_i$. According to the definition in eq. (2), $s'_{i,j}$ will be negative if an increase of resistivity in the element Ω_j results in a decrease of the apparent resistivity $\hat{\rho}_i$.

3.1 Normal or potential configuration

The normal configuration consists of two electrodes in the borehole. The potential field generated by the current injection in electrode A is recorded by a single potential electrode M. The reference level for displaying the measured apparent resistivity in depth is defined as being half way between A and M. In the example in Fig. 3(a), the distance $\overline{AM}$ is equal to $10r_0$.

An obvious feature is the symmetry of the sensitivity pattern regarding the reference level. This property results from the reciprocity, which means that interchanging electrodes A and M gives the same reading. In the homogeneous space ($\rho_t/\rho_0 = 1$), the sensitivity between the two electrodes becomes negative. The negative zone extends up to five borehole radii into the rock formation. A high sensitivity gradient is observed near the positions of the electrodes.

The image for the ratio 0.1 is similar. The negative zone is slightly expanded and the contrast becomes sharper. In the case of a ratio of 10, the situation changes significantly. The negative zone disappears completely and the absolute values of sensitivity become much smaller. The main feature for the ratio of 100 is a sensitivity decrease in a radial direction. A depth structure in the sensitivity image is hardly visible with the exception of two slight maxima in the vicinity of the electrode positions.

If the resistivity ratio ρ_t/ρ_0 increases a larger part of the injected current will flow in the mud along the borehole and does not enter in the formation. Consequently, the extension of areas of larger sensitivity (e.g. $s' > 1.25$) into the formation decreases.

3.2 Lateral or gradient configuration

The lateral configuration consists of three electrodes in the borehole. The electrodes M and N measure the potential difference of the field caused by current injection at electrode A. The reference level for the measured apparent resistivity is defined at the depth of the centre between M and N. If the distance between M and N becomes sufficiently small, the potential difference divided by the distance approximates the vertical gradient of the potential field, which is related to the mean value of the vertical component of the electric field. Fig. 3(b) shows the sensitivity image for $\overline{AM} = 8r_0$ and $\overline{MN} = 2r_0$.

In the homogeneous case ($\rho_t/\rho_0 = 1$), three different parts can be distinguished. The main feature is a zone of negative sensitivity between the injection electrode A and the first potential electrode M. This part extends up to three borehole radii into the formation. A second area of negative sensitivity is located above the potential electrode N, it extends radially over the whole volume. All other parts show positive sensitivity with maximal values between the two potential electrodes and below the injection electrode. A distinct gradient of sensitivity is found near the positions of the electrodes.

For a contrast of 0.1 the pattern is very similar. The sensitivity gradients are steeper and the negative parts become slightly greater. The situation changes for a ratio of 10. The negative part between A and M disappears. Only a slight vertical change of positive sensitivity is observed at the potential electrode positions. The zone of negative sensitivity above N remains nearly unchanged. However, the line of zero sensitivity is slightly shifted from the electrode position N down towards the position of electrode M. For a contrast of 100, zero sensitivity is moved further downwards and the vertical sensitivity contrast becomes lower again.

3.3 Second-difference configuration

The second difference approximates the second vertical derivative of the potential field. This quantity, which can be calculated from two gradient readings, is an appropriate indicator of current flow in the radial direction. The reference level corresponds to the depth

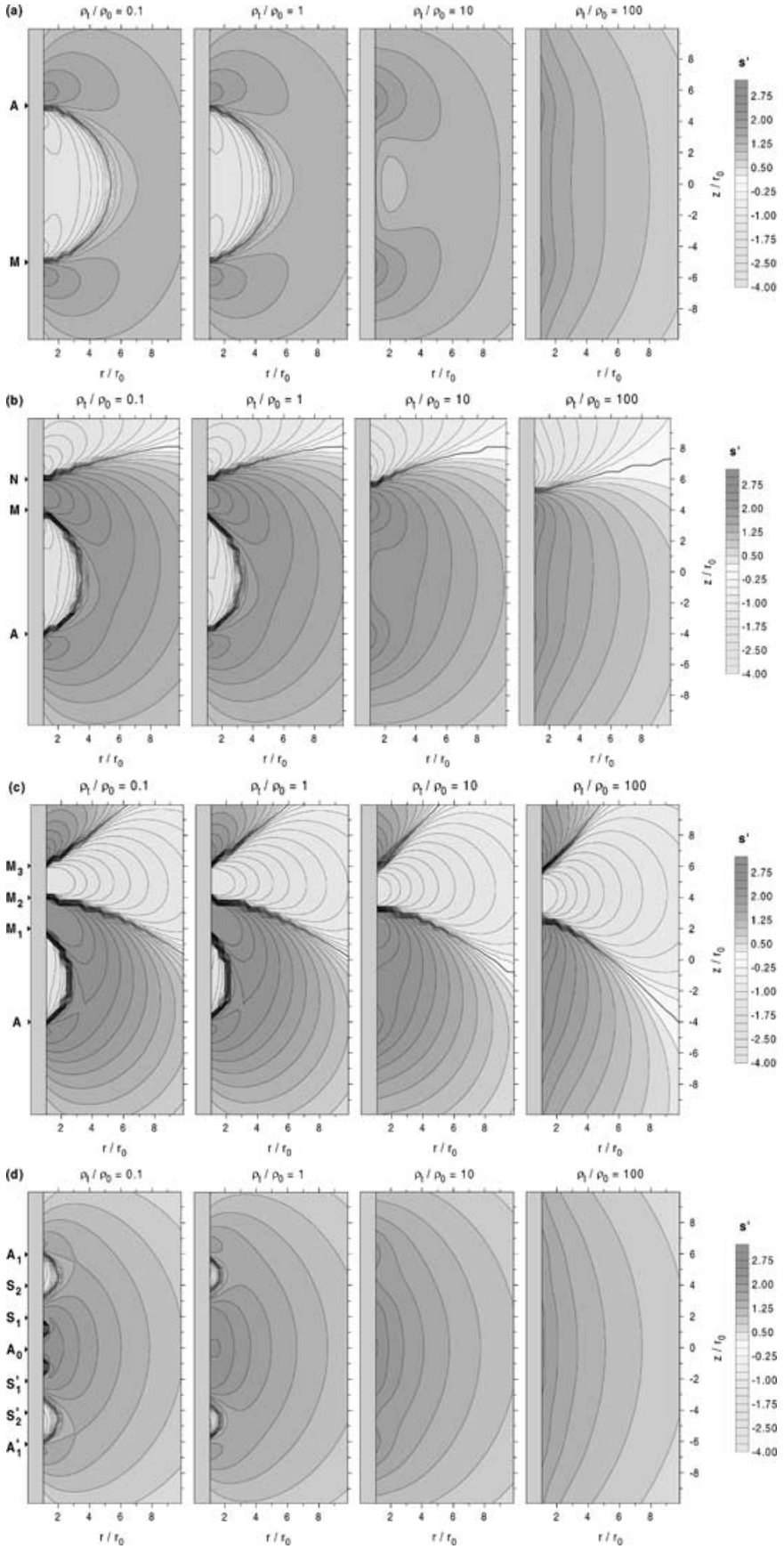

Figure 3. Distribution of sensitivity parameter s' for four resistivity ratios ρ_t/ρ_0. (a) Normal configuration, $\overline{AM} = 10r_0$. (b) Lateral configuration, $\overline{AM} = 8r_0$, $\overline{MN} = 2r_0$. (c) Second-difference configuration, $\overline{AM_1} = 6r_0$; $\overline{M_1M_2} = \overline{M_2M_3} = 2r_0$. (d) Laterolog-7 configuration, electrodes spaced at $2r_0$.

of electrode M_2. The geometry of the configuration in Fig. 3(c) represents $\overline{AM_1} = 6r_0$ and $\overline{M_1M_2} = \overline{M_2M_3} = 2r_0$.

The lower part (below M) of the sensitivity pattern for the homogeneous case ($\rho_t/\rho_0 = 1$) looks similar to that for the gradient configuration. However, above the second potential electrode M_2, there is another change of sign at the position of the third potential electrode M_3. The zone of negative sensitivity is funnel-shaped with its centre being between electrodes M_2 and M_3. This configuration shows the most distinct contrast between positive and negative sensitivity.

The trends for the other ratios ρ_t/ρ_0 are similar to that for $\rho_t/\rho_0 = 1$. The zone of negative sensitivity between the injection electrode and the first potential electrode disappears with increasing contrast. The lines of zero sensitivity are shifted. Compared with the other configurations, the sensitivity contrast becomes only slightly smaller with increasing resistivity contrast.

3.4 Laterolog-7

Fig. 3(d) shows the sensitivity images for a focused resistivity tool consisting of seven electrodes that are equally spaced. The electrode spacing is equal to $2r_0$. The two outer injection electrodes A_1' and A_1, which are called guard electrodes, have the same polarity as the central injection electrode A_0. The focusing or bucking currents are chosen in such a way that the two potential differences between the pairs of monitoring electrodes S_1, S_2 and S_1', S_2' become zero. This condition is necessary to impede a flow of current parallel to the tool through the borehole mud. Consequently, the current will be focused into the formation. The reference level corresponds to the depth of the central electrode A_0. The symmetry of the array results in a symmetric sensitivity distribution in z about the reference level. The bucking currents which depend on the resistivity contrast are determined by a forward modelling algorithm.

In the homogeneous space ($\rho_t/\rho_0 = 1$), the sensitivity image is characterized by three different areas. There are two parts with negative sensitivity between the guard electrodes A_1' or A_1 and their two neighbouring potential electrodes. These negative parts extend only up to one borehole radius into the formation. An area of increased sensitivity is centred around the current electrode A_0.

In the case of a resistivity contrast of 0.1, two additional zones of negative sensitivity appear, both between electrode A_0 and the neighbouring electrodes S_1' and S_1, respectively. For a contrast of 10, the negative zones disappear and the sensitivity is increased slightly at the positions of the guard electrodes. An increase of sensitivity around the central injection electrode A_0 is also observed. In the case of a contrast of 100, the variation in the vertical direction becomes smaller. Only around the central region of the configuration can a slightly increased sensitivity be seen, but the absolute value decreases.

4 VERTICAL RESOLUTION

The sensitivity images can be used to assess the vertical resolution of the different electrode configurations for detecting various geological structures. First, a thin layer is assumed. The second example examines a layer thickness, which corresponds to $6r_0$. The results are compared with a numerical modelling by a finite-difference code.

4.1 Sensitivity of a thin layer

A thin layer with a thickness of $\Delta z = 0.1r_0$ is chosen. The sensitivity values shown in the preceding section are summed up in the radial direction starting at the borehole wall up to a distance of 15 borehole radii from the axis. The resulting values correspond to the sensitivity of a thin layer. Since the thin-layer sensitivity also varies with the resistivity ratio ρ_t/ρ_0 the following figures show the curves for the configurations investigated and the four different resistivity ratios. The curves reflect qualitatively the logging response of a thin resistive layer. It should be noted that the sensitivity scale varies for the different configurations.

The curves of thin-layer sensitivity for a normal configuration are presented in Fig. 4(a). For low resistivity contrast ($\rho_t/\rho_0 < 5$), the resulting sensitivity becomes negative between electrodes A and M. This behaviour causes the well-known resistivity inversion effect: thin resistive layers are characterized by a crater structure (Pirson 1963) consisting of a central resistivity minimum with two adjacent maxima. A thin conductive layer is displayed as a local maximum between two minima. Since the layer sensitivity remains positive for larger contrasts the inversion effect does not occur in this case.

The curves of a gradient array shown in Fig. 4(b) are characterized by a maximum of thin-layer sensitivity between potential electrodes M and N. With increasing resistivity contrast, this maximum approaches electrode M and the change from positive to negative sensitivity occurs between the potential electrodes. The second maximum, which is called the *shadow peak* (Pirson 1963), near the current electrode A is flattened. On the low contrast curves the sensitivity approaches zero in the section between electrodes A and M, which is called the *death zone* (Pirson 1963).

In the case of the second-difference configuration as shown in Fig. 4(c), the amplitudes of the thin-layer sensitivity curves decrease with increasing resistivity contrast, too. The portion of current that enters the formation is reduced with increasing formation resistivity. The change from maximum to minimum sensitivity occurs between potential electrodes M_1 and M_3. For the highest contrast, only a minimum is preserved. The local maximum near the current electrode disappears.

The thin-layer sensitivity of the Laterolog-7 (Fig. 4d) is symmetric and remains positive for all resistivity contrasts considered. No inversion effect is observed. The sensitivity maximum corresponds to the centre of the array.

4.2 Power of resolution

The thin-layer sensitivity can also be used to assess the resolution power of different configurations. Assuming a hypothetical logging tool with an ideal resolution, a thin layer should be reflected by a sharp pulse in the logging curve. The amplitude should correspond to the true formation resistivity and the width of the pulse should be equal to the layer thickness. As the thin-layer sensitivity curves in Fig. 4 show, the response of real electrical logging curves looks more complicated. In order to assess the resolution power for all investigated configurations and resistivity ratios ρ_t/ρ_0, three quantities are compiled in Table 1: the maximum thin-layer sensitivity s_{max}, the half-width $z_{1/2}$ and a resolution parameter q. The half-width corresponds to half the distance between the depth values with half-maximum amplitude. A vertical bar indicates the distance $2z_{1/2}$ in Fig. 4. In the case of the second-difference configuration, the thin-layer sensitivity values are multiplied by -1 to obtain a significant maximum for all contrasts. The higher the maximum amplitude and the smaller the half-width the sharper the signal in the electrical logging curve and the better the resolution power. Therefore, the parameter

$$q = \frac{s_{max}}{z_{1/2}} \tag{14}$$

has been defined to assess the resolution power.

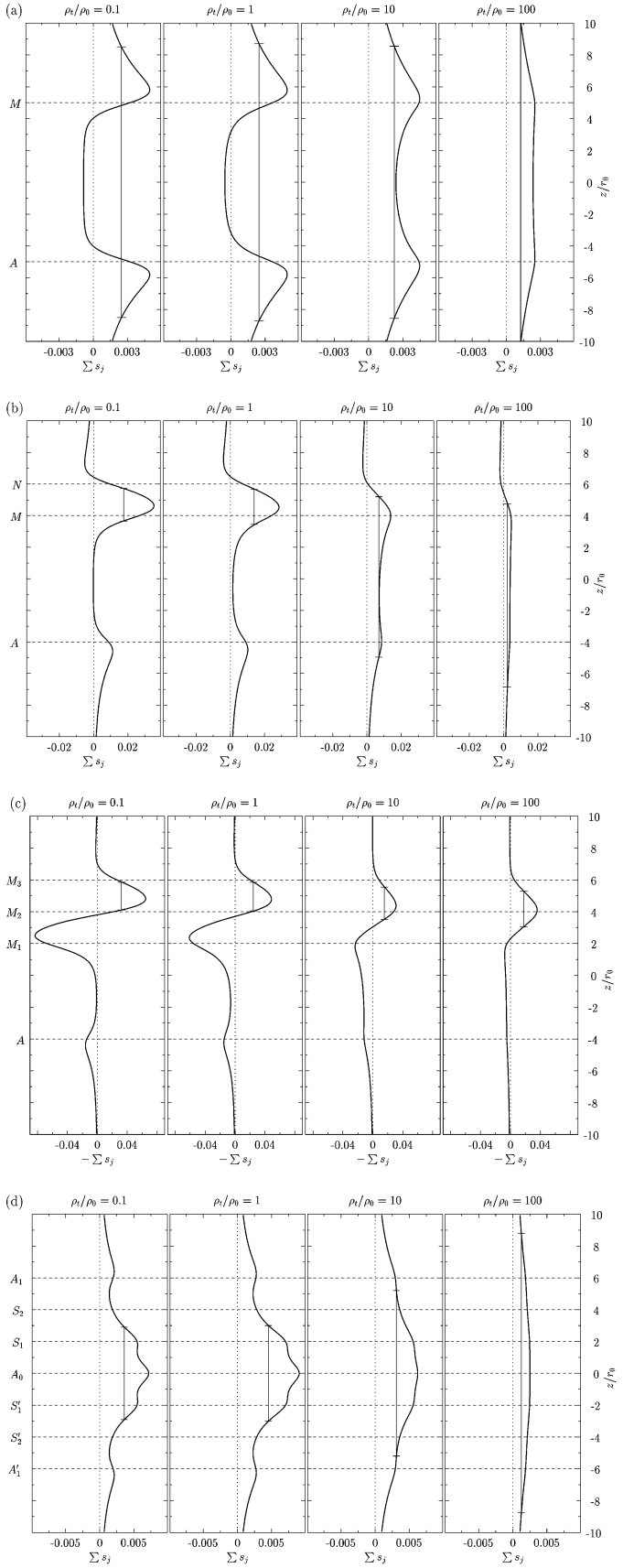

Figure 4. Thin-layer ($\Delta z = 0.1 r_0$) sensitivity for four resistivity ratios ρ_t/ρ_0. The vertical bar denotes the double half-width $z_{1/2}$. (a) Normal configuration, $\overline{AM} = 10 r_0$. (b) Lateral configuration, $\overline{AM} = 8 r_0$, $\overline{MN} = 2 r_0$. (c) Second-difference configuration, $\overline{AM_1} = 6 r_0$; $\overline{M_1 M_2} = \overline{M_2 M_3} = 2 r_0$. (d) Laterolog-7 configuration, electrodes spaced at $2 r_0$.

Table 1. Maximum sensitivity, half-width and resolution parameter of a thin layer ($\Delta z = 0.1 r_0$) for all investigated configurations and resistivity ratios ρ_t/ρ_0.

Configuration	ρ_t/ρ_0	Layer sensitivity maximum $s_{max} \times 10^3$	Half-width $z_{1/2}$ in r_0	Resolution parameter $q \times 10^3$ in $1/r_0$
Normal	0.1	4.950	8.5	0.582
	1	4.929	8.7	0.567
	10	4.466	8.55	0.522
	100	2.500	10.1	0.248
Lateral	0.1	35.295	1.04	33.938
	1	28.480	1.1	25.891
	10	13.912	5.08	2.738
	100	4.592	5.8	0.792
Second difference	0.1	64.614	0.88	73.425
	1	48.764	0.9	54.182
	10	31.021	1.02	30.412
	100	35.699	1.13	31.592
Laterolog-7	0.1	7.166	2.9	2.471
	1	9.048	3.0	3.016
	10	6.238	5.2	1.200
	100	2.510	8.78	0.286

From Table 1 it can be concluded that the second-difference configuration yields the best resolution in the case of thin layers. The changes of the resolution parameter q with varying resistivity ratio ρ_t/ρ_0 is only moderate. Even for a high resistivity contrast, a thin layer can be resolved. This property of second differences is used to detect layer boundaries (Hakvoort *et al.* 1998).

As is known from conventional resistivity logging, the lateral tool possesses a better ability to resolve thin layers compared with a normal configuration. However, the comparison in Table 1 shows that the resolution parameter q of the lateral array decreases significantly with increasing resistivity contrast ρ_t/ρ_0.

The focused resistivity arrays yield a good resolution if the layer thickness reaches at least the width of the focused current beam. For the Laterolog-7 tool used in this investigation, the beamwidth of $6r_0$ exceeds the true thin-layer thickness by a factor of 60. Therefore, the focusing results in only a slight improvement of the resolution parameter q compared with that of the normal configuration and the advantage of focusing vanishes at higher ratios ρ_t/ρ_0. Only taking into account the foregoing investigation, the thin-layer resolution of a Laterolog-7 seems to be inferior to that of the lateral or second-difference configuration. This conclusion may be modified considering the results of the next section.

4.3 Comparison with numerical forward modelling

For a further investigation, a layer thickness of $6r_0$ is used. This layer thickness corresponds to the beamwidth of the Laterolog-7 selected in this study.

According to eq. (2) the change in apparent resistivity $\Delta\hat{\rho}_i$ measured by the configuration i can be approximated from a given change in the resistivity of a certain region $\mathcal{L}$ in the model by the relation

$$\Delta\hat{\rho}_i \approx \sum_{\Omega_j \in \mathcal{L}} s_{i,j} \Delta\rho_j, \tag{15}$$

where the summation is done over all volume elements Ω_j that belong to this region $\mathcal{L}$. If $\Delta\rho_j$ is given as the relative change of resistivity of an embedded layer compared with the adjacent formation the variation of the resulting apparent resistivity $\Delta\hat{\rho}_i$ is also a relative quantity. Models with a relative difference in layer resistivity of $+10$, $+50$, $+100$ per cent (resistive layers), or -9, -33 and -50 per cent (conductive layers) are chosen.

The relative changes of apparent resistivity are calculated by applying the sensitivity distribution according to eq. (15). Since the resistivity is constant within a layer, first, the summation of sensitivity is performed over all elements of the layer. Then, the resulting layer sensitivity is multiplied by the relative change $\Delta\rho_{\mathcal{L}}$.

The linearization expressed by eq. (15) is only valid for small changes in the resistivity model. Several authors use low-contrast approximations for forward modelling and inversion of resistivity data (Beard *et al.* 1996; Brunner *et al.* 1999). The aim of this investigation is to show the limits of the low-contrast approximation for modelling of resistivity logging.

A logging curve can be designed by plotting the calculated changes of apparent resistivity $\Delta\hat{\rho}_i$ as a function of the shift between the centre of configuration and the centre of the layer. The curves are compared with the results of a numerical forward modelling by a finite-difference code (Weller 1986) that considers the same layered models.

Though the investigation has been performed with the same set of four different resistivity ratios between mud and formation, only a single resistivity ratio ($\rho_t/\rho_0 = 10$) is selected for the graphical presentation. Fig. 5(a) shows the results for the normal configuration with electrodes as depicted on the left-hand margin. The solid lines correspond to the changes computed with the sensitivity approximation of eq. (15), the dashed lines to the results of the forward modelling. The shape of the curves shows a crater-like structure between electrodes A and M which is in agreement with the behaviour of a thin layer. In this case, the layer thickness ($6r_0$) is smaller than the electrode distance $\overline{AM} = 10r_0$. The sensitivity curves for a relative difference in layer resistivity of $+10$ and -9 per cent are close to those of the forward modelling. Also for $+50$ and -33 per cent, the agreement is fairly good. As expected from a linear approximation, the higher the contrast between the resistivity of the layer and that of the homogeneous formation the greater the differences between the curves. The method using the sensitivity distribution overestimates the true changes in apparent resistivity for resistive layers with a relative difference in layer resistivity of >10 per cent. Yet, the absolute changes are underestimated for conductive layers.

The lateral (Fig. 5b) and the second-difference configuration (Fig. 5c) show similar features as found for the normal configuration:

(1) a small difference in layer resistivity results in nearly identical curves for the sensitivity approximation and forward modelling;
(2) a greater relative difference causes stronger deviations;
(3) for resistive layers, the changes are overestimated by the sensitivity approximation;
(4) for conductive layers, the relative changes are underestimated.

The different scales of the $\Delta\hat{\rho}$ axis should be noted. An increase of the maximum is observed proceeding from the potential, over lateral to second-difference configuration curves. An interesting property is observed for the second-difference configuration. The distance between the maxima and the minima of the curves corresponds approximately to the layer thickness of $6r_0$. This property can be used to derive the location of layer boundaries.

The situation for the Laterolog-7 tool seems to be more complicated. In Fig. 5(d), the curves resulting from the sensitivity

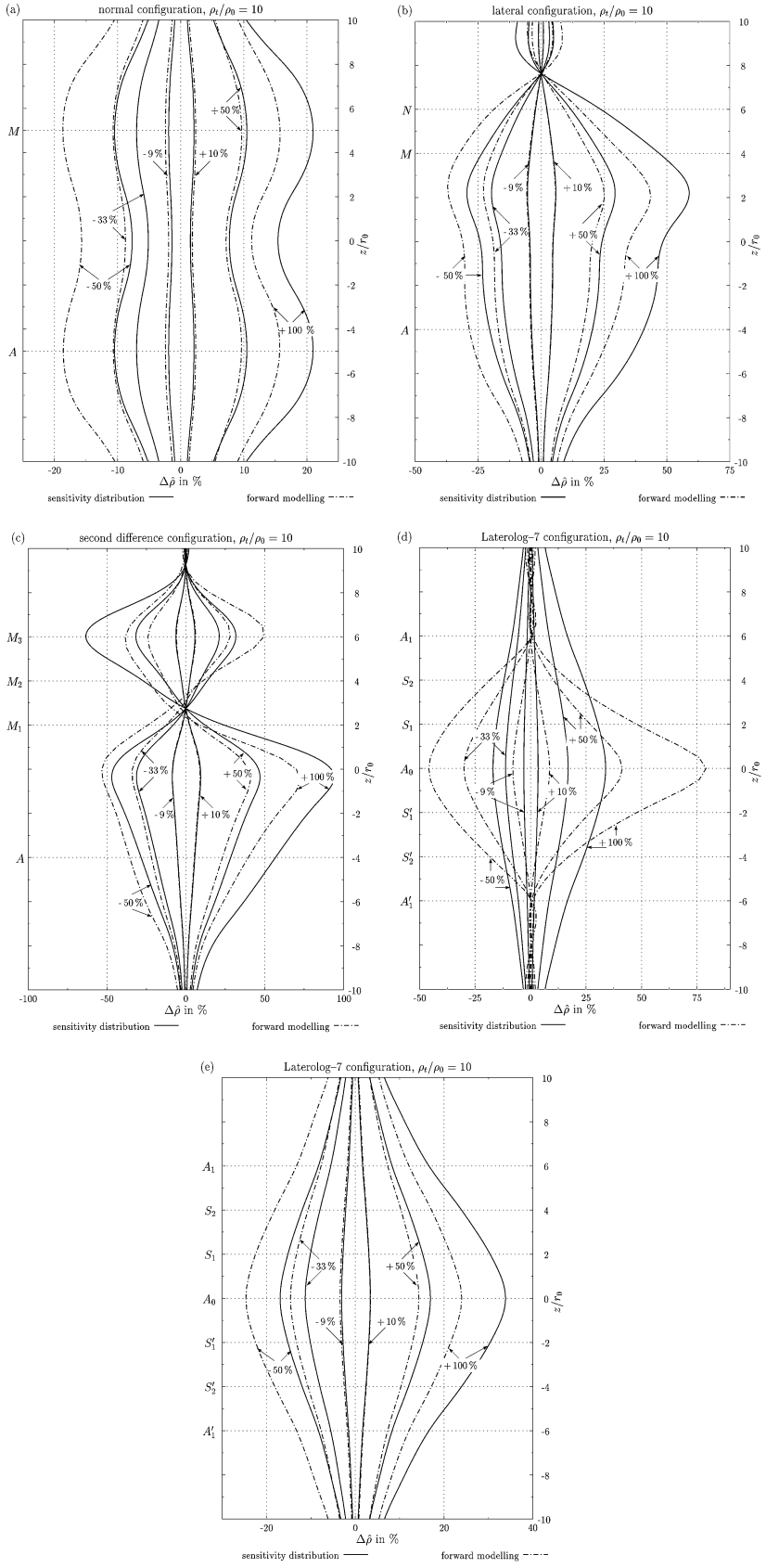

Figure 5. Comparison between the sensitivity approximation and the numerical forward modelling of a layer with a thickness of $6r_0$ and six different relative resistivity contrasts and a resistivity ratio $\rho_t/\rho_0 = 10$. (a) Normal configuration, $\overline{AM} = 10r_0$. (b) Lateral configuration, $\overline{AM} = 8r_0$, $\overline{MN} = 2r_0$. (c) Second-difference configuration, $\overline{AM_1} = 6r_0$; $\overline{M_1M_2} = \overline{M_2M_3} = 2r_0$. (d) Laterolog-7 configuration with varying bucking currents in forward modelling, electrodes spaced at $2r_0$. (e) Laterolog-7 configuration with fixed bucking currents in forward modelling, electrodes spaced at $2r_0$.

approximation are flat compared with the curves calculated by numerical forward modelling that show more accentuated maxima. Even for small changes, the differences are significant. The maxima of apparent resistivity are severely underestimated by the sensitivity approximation. The differences are caused by the current ratios. In the forward modelling, the bucking currents are adapted to the true resistivity structure, ensuring that the potential differences between the two pairs of monitoring electrodes are zero. Since in our focused tool no pairs of electrodes are shorted, two different bucking currents are calculated. A special study has shown that the use of a constant geometrical factor (Jackson 1981) yields better results for this version of a Laterolog-7 compared with the variable geometric factor as proposed by Roy & Dutta (1993).

The sensitivity approximation does not take into account variations of the bucking currents. It assumes a fixed current ratio that is predetermined for a homogeneous formation. As shown in Fig. 5(e), the use of constant bucking currents in the forward modelling calculation of focused curves results in a *static* response that becomes comparable with the curves resulting from the sensitivity approximation.

As can be seen from a comparison between Figs 5(d) and (e), the real focusing effect is only achieved by considering the appropriate choice of the bucking currents. Compared with the *static* response of a focused tool in Fig. 5(e), the *dynamic* response of the forward modelling with varying bucking currents (Fig. 5d) shows the real power of focused tools.

The maximum and mean differences between the logging curves resulting from forward modelling and the linearization according to eq. (15) are shown in Table 2. Since a reliable modelling of the Laterolog-7 response is not possible using the linear approximation, this configuration will not be discussed. The other data confirm that the linearization can be applied as a low-contrast approximation. A resistivity contrast of 1.1 causes deviations of less than 1 per cent between the finite-difference model and the linear approximation. The deviation increases by up to 25 per cent for a resistivity contrast of 2. The approximation works best for the normal configuration and it becomes worse for lateral and second-difference configuration. Since the contrast of layer resistivities in most wells is greater than 2, the application of the low-contrast approximation should remain the exception.

The results of all investigated resistivity ratios between mud and formation are compiled in Table 3. The maximum of the resistivity change $\Delta\hat{\rho}_{\max}$ and the half-width $z_{1/2}$ are derived from forward modelling for an embedded layer with a relative resistivity difference of $+100$ per cent with respect to the adjacent formation. The resolution parameter q is determined as the ratio between $\Delta\hat{\rho}_{\max}$ and $z_{1/2}$. Compared with the very thin layer in Table 1 with a thickness of $0.1r_0$, the resolution parameter has increased strongly for a layer with a thickness of $6r_0$. However, the factor of 60 corresponding to the thickness ratio is only exceeded by the Laterolog-7. The poor resolution of the normal configuration for a layer thickness smaller than the electrode spacing is confirmed by this investigation. A better resolution is achieved by a lateral or second-difference configuration. However, the resolution deteriorates with increasing resistivity ratio ρ_t/ρ_0 because part of the current flow is restricted to the borehole. Since the focused tool forces the current to enter into the formation Laterolog-7 is not affected by this resistivity ratio.

Table 2. Maximum and mean differences between the resistivity logging curves calculated by finite-difference forward modelling and using the linear approximation for an embedded layer with a thickness of $6r_0$ and a resistivity ratio $\rho_t/\rho_0 = 10$.

Configuration	Relative resistivity difference in per cent	Maximum difference in per cent	Mean difference in per cent
Normal	−50	8.2	7.6
	−33	3.7	3.4
	−9	0.5	0.5
	+10	0.3	0.3
	+50	0.9	0.6
	+100	5.3	4.2
Lateral	−50	9.0	6.2
	−33	3.7	2.6
	−9	0.3	0.2
	+10	0.1	0.1
	+50	4.5	2.8
	+100	15.7	9.8
Second	−50	18.7	7.0
difference	−33	7.1	2.7
	−9	0.5	0.2
	+10	0.3	0.2
	+50	7.7	3.9
	+100	25.0	12.8
Dynamic	−50	28.9	11.1
Laterolog-7	−33	18.9	6.8
	−9	4.9	1.7
	+10	5.2	1.7
	+50	24.5	7.9
	+100	45.2	14.6
Static	−50	7.7	5.5
Laterolog-7	−33	3.3	2.4
	−9	0.4	0.3
	+10	0.1	0.1
	+50	2.6	1.3
	+100	9.9	5.6

5 RESULTS AND CONCLUSIONS

The sensitivity distribution of different electrode configurations has proved to be an appropriate tool for analysing the resolution capabilities of electrical logging tools. Since the sensitivity pattern depends on the resistivity model in the borehole environment, the sensitivity for a homogeneous media can only give a rough approximation. The sensitivity distribution considering the resistivity contrast between a mud-filled borehole and formation allows a more reliable assessment of the resolution power of a certain configuration for different mud or formation resistivities.

The sensitivity can also be used for an approximate forward modelling—the smaller the contrast the better the agreement with the numerical forward modelling. If the resistivity contrast reaches a factor of 2 the resulting response only qualitatively reflects the main features of the logs. The accuracy of this low-contrast approximation is no longer sufficient for a quantitative interpretation.

In the case of focused tools the sensitivity pattern does not consider the effect of the varying bucking currents. However, the focusing effect is only achieved by an appropriate choice of the bucking currents. A constant bucking current results in a *static* response that does not reach the resolving power of a real focused tool.

The numerical study has confirmed the advantages of Laterolog-7 in comparison with normal configurations as pointed out by Roy & Dutta (1993):

(1) the apparent resistivity anomaly becomes sharper;

(2) the apparent resistivity curve shows a monotonic rise or fall across a contact;

Table 3. Results of numerical forward modelling: maximum resistivity change, half-width and resolution parameter of a layer with a thickness of $6r_0$ and a relative resistivity contrast of +100 per cent for all investigated configurations and resistivity ratios ρ_t/ρ_0.

Configuration	ρ_t/ρ_0	Normalized resistivity change maximum $\Delta\hat{\rho}_{max} \times 10^3$	Half-width $z_{1/2}$ in r_0	Resolution parameter $q \times 10^3$ in $1/r_0$
Normal	0.1	157.17	11.75	13.37
	1	161.79	11.75	13.76
	10	156.97	11	14.27
	100	93.73	12	7.81
Lateral	0.1	605.44	2.75	220.16
	1	574.54	3	191.51
	10	430.50	5.5	78.27
	100	148.95	6	24.83
Second difference	0.1	791.85	1.15	688.56
	1	601.50	1.3	462.69
	10	384.56	2	192.28
	100	452.44	2.75	164.52
Static Laterolog-7	0.1	291.45	3.75	77.72
	1	368.72	4.25	86.75
	10	239.65	6.0	39.94
	100	93.51	10.0	9.35
Dynamic Laterolog-7	0.1	476.22	2.7	176.38
	1	846.63	2.4	352.76
	10	790.54	2.5	316.22
	100	755.84	2.5	302.34

(3) the bucking current logs can be used for a sharper delineation of bed boundaries;

(4) the curves are suitable for delineating thin layers.

The last item is valid if the layer thickness reaches at least the order of the beamwidth. The tool design should consider this property in order to obtain the required resolution.

The design of sophisticated multi-electrode resistivity tools involves investigation of the resolution power and the ability to detect several geological or borehole features. The choice of electrode positions and the manner combining them for data acquisition influences the resolution of the tool. The inversion of logging data can only extract information that has been gathered by the sets of different configurations.

An accurate and fast algorithm for determining the sensitivity distribution is the basis of any efficient inversion programme. Our aim in more recent work has been the further improvement of the inversion algorithm for the data of a multi-electrode resistivity tool. The tool design and the results of the inversion will be reported in a forthcoming paper.

ACKNOWLEDGMENTS

This work was carried out in co-operation with the firm Brunnen- und Bohrlochinspektion GmbH within the framework of a project that is supported by the Federal Ministry of Economics and Technology (BMWi). We are very grateful to B. Singer and an anonymous reviewer for their useful comments and suggestions.

REFERENCES

Abramowitz, M. & Stegun, I.A., 1965. *Handbook of Mathematical Functions,* Dover, New York.

Barker, R.D., 1979. Signal contribution sections and their use in resistivity studies, *Geophys. J. R. astr. Soc.,* **59,** 123–129.

Beard, L.P., Hohmann, G.W. & Tripp, A.C., 1996. Fast resistivity/IP inversion using a low-contrast approximation, *Geophysics,* **61,** 169–179.

Brunner, I., Friedel, S., Jacobs, F. & Danckwardt, E., 1999. Investigation of a Tertiary maar structure using three-dimensional resistivity imaging, *Geophys. J. Int.,* **136,** 771–780.

Dakhnov, V.N., 1962. Geophysical well logging, *Q. Colorado School Mines,* **57,** 180.

Fan, X., 1998. Modellierung und Inversion von gleichstromelektrischen Bohrlochmessungen mit 2D- und 3D-Finite-Differenzen, Berlin, Techn. Univ., *Dissertation*.

Hakvoort, R.G., Fabris, A., Frenkel, M.A., Koelman, J.M.V.A. & Loermans, A.M., 1998. Field measurements and inversion results of the high-definition lateral log, *39th Ann. SPWLA meeting*.

Jackson, P.D., 1981. Focussed electrical resistivity arrays: some theoretical and practical experiments, *Geophys. Prospect.,* **29,** 601–626.

Kampke, A., 1999. Focused imaging of electrical resistivity data in archaeological prospecting, *J. App. Geophys.,* **41,** 215–227.

Loke, M.H. & Barker, R.D., 1996. Rapid least-squares inversion of apparent resistivity pseudosections by quasi-Newton method, *Geophys. Prospect.,* **44,** 131–152.

Pirson, S.J., 1963. *Handbook of Well Log Analysis,* Prentice-Hall, Englewood Cliffs, NJ.

Roy, K.K. & Dutta, D.J., 1993. Analysis of a laterolog tool with variable geometric factor, *Log Anal.,* **34,** 24–32.

Schön, J. & Weller, A., 1984. Calculation of synthetic resistivity curves by finite-difference method and approximate focusing filter operation, *Trans. 9th Int. Formation Evaluation Symp.,* paper 23.

Seichter, M., 1998. Rekonstruktion der räumlichen Verteilungen komplexer elektrischer Leitfähigkeiten, Braunschweig, Techn. Univ., *Dissertation*.

Spitzer, K., 1998. The three-dimensional DC sensitivity for surface and subsurface sources, *Geophys. J. Int.,* **134,** 736–746.

Weller, A., 1986. Berechnung geoelektrischer Potentialfelder mit dem Differenzenverfahren, *Freib. Forsch.-H., C,* **405,** 68–122.

Weller, A., Gruhne, M., Seichter, M. & Börner, F.D., 1996. Monitoring hydraulic experiments by complex conductivity tomography, *E. J. Env. Eng. Geophys.,* **1,** 209–228.

APPENDIX A: POTENTIAL IN THE CASE OF A CYLINDRICAL COAXIAL BOUNDARY

Dakhnov (1962) gave a description for solving the forward problem for the case of cylindrical coaxial boundaries. Forward modelling requires the knowledge of the potential at the borehole axis $V(0, z)$. Although our aim is different, we use a similar approach. For convenience, all coordinates are expressed in terms of the borehole radius r_0, i.e. $\hat{r} = r/r_0$ and $\hat{z} = z/r_0$. The potential function

$$V(\hat{r}, \hat{z}) = \begin{cases} V_0(\hat{r}, \hat{z}) & \hat{r} < 1 \\ V_t(\hat{r}, \hat{z}) & \hat{r} \geq 1 \end{cases}$$

must satisfy the following requirements.

(1) Outside the current injection point that is placed at the origin, the Laplace equation

$$\nabla^2 V(\hat{r}, \hat{z}) = 0 \tag{A1}$$

is satisfied. Since axial symmetry is assumed, the Laplace equation in cylindrical coordinates reduces to

$$\frac{\partial^2 V(\hat{r}, \hat{z})}{\partial r^2} + \frac{1}{r}\frac{\partial V(\hat{r}, \hat{z})}{\partial r} + \frac{\partial^2 V(\hat{r}, \hat{z})}{\partial z^2} = 0. \tag{A2}$$

(2) At large distances from the injection point the potential vanishes:

$$\lim_{R \to \infty} V(\hat{r}, \hat{z}) = 0 \tag{A3}$$

with $R = \sqrt{\hat{r}^2 + \hat{z}^2}$.

(3) In the vicinity of the current source, the potential is approximated by the potential of the homogeneous space with the resistivity ρ_0,

$$\lim_{R\to 0} V_0(\hat{r},\hat{z}) = \frac{\rho_0 I}{4\pi R r_0}. \tag{A4}$$

(4) The potential is continuous at $\hat{r}=1$ (first boundary condition):

$$V_0(\hat{r},\hat{z})|_{\hat{r}=1} = V_t(\hat{r},\hat{z})|_{\hat{r}=1}\,. \tag{A5}$$

(5) The current density is continuous at $\hat{r}=1$ (second boundary condition):

$$\frac{1}{\rho_0}\frac{\partial V_0(\hat{r},\hat{z})}{\partial r}\bigg|_{\hat{r}=1} = \frac{1}{\rho_t}\frac{\partial V_t(\hat{r},\hat{z})}{\partial r}\bigg|_{\hat{r}=1}. \tag{A6}$$

(6) Since the current is injected at $z=0$ the potential is symmetric in z about the origin

$$V(\hat{r},\hat{z}) = V(\hat{r},-\hat{z}), \tag{A7}$$

a separation approach

$$V(\hat{r},\hat{z}) = f(\hat{r})\cdot g(\hat{z}) \tag{A8}$$

is used to solve eq. (A2). It results in two separate differential equations:

$$\frac{g''(\hat{z})}{g(\hat{z})} = -m^2 \tag{A9}$$

and

$$f''(\hat{r}) + \frac{1}{\hat{r}} f'(\hat{r}) - m^2 f(\hat{r}) = 0. \tag{A10}$$

The particular solution of eq. (A9) are the sine and cosine functions. The sine function can be excluded because of the symmetry condition (A7). The solution of the Bessel differential equation (A10) are the Bessel functions of first and second kind of zero order. The complete solution must have the form:

$$V(\hat{r},\hat{z}) = \int_0^\infty [A(m)I_0(m\hat{r}) + B(m)K_0(m\hat{r})]\cos(m\hat{z})\,dm. \tag{A11}$$

Considering condition (A4) and the Weber–Lipschitz formula, the solution in the borehole results in

$$V_0(\hat{r},\hat{z}) = \frac{\rho_0 I}{2\pi^2 r_0}\int_0^\infty [K_0(m\hat{r}) + C_0(m)I_0(m\hat{r})]\cos(m\hat{z})\,dm. \tag{A12}$$

In the undisturbed formation, the potential V_t cannot contain the term $I_0(m\hat{r})$ which tends to become infinite for large values of the argument $\hat{r}$. Using an analogous preceding factor, the solution in the undisturbed formation may be given in the form:

$$V_t(\hat{r},\hat{z}) = \frac{\rho_t I}{2\pi^2 r_0}\int_0^\infty D_t(m)K_0(m\hat{r})\cos(m\hat{z})\,dm. \tag{A13}$$

The two unknown functions $C_0(m)$ and $D_t(m)$ are determined by applying the boundary conditions (A5) and (A6):

$$\rho_0[C_0(m)I_0(m) + K_0(m)] = \rho_t D_t(m)K_0(m), \tag{A14}$$

$$C_0(m)I_1(m) - K_1(m) = -D_t(m)K_1(m) \tag{A15}$$

with $I_1(x) = dI_0(x)/dx$ and $K_1(x) = -dK_0(x)/dx$ are the Bessel functions of the first order. Using these identities, the functions are:

$$C_0(m) = \frac{(\rho_t/\rho_0 - 1)\,K_0(m)K_1(m)}{I_0(m)K_1(m) - (\rho_t/\rho_0)I_1(m)K_0(m)}, \tag{A16}$$

$$D_t(m) = \frac{I_1(m)K_0(m) + I_0(m)K_1(m)}{(\rho_t/\rho_0)I_1(m)K_0(m) + I_0(m)K_1(m)}. \tag{A17}$$

The spatial derivatives of the potential are:

$$\frac{\partial V_t(\hat{r},\hat{z})}{\partial r} = \frac{-\rho_t I}{2\pi^2 r_0^2}\int_0^\infty D_t(m)K_1(m\hat{r})m\cos(m\hat{z})\,dm, \tag{A18}$$

$$\frac{\partial V_t(\hat{r},\hat{z})}{\partial z} = \frac{-\rho_t I}{2\pi^2 r_0^2}\int_0^\infty D_t(m)K_0(m\hat{r})m\sin(m\hat{z})\,dm. \tag{A19}$$

Using the periodic behaviour of the sine and cosine functions, the substitution $m = n + 2k\pi/\hat{z}$ yields the formulae to determine numerically the value of the derivatives:

$$\frac{\partial V_t(\hat{r},\hat{z})}{\partial r} = \frac{-\rho_t I}{2\pi^2 r_0^2}\int_0^{2\pi/\hat{z}}\cos(n\hat{z})\sum_{k=0}^{\infty}[D_t(n+2k\pi/\hat{z}) \times (n+2k\pi/\hat{z})K_1(n\hat{r}+2k\pi\hat{r}/\hat{z})]\,dn, \tag{A20}$$

$$\frac{\partial V_t(\hat{r},\hat{z})}{\partial z} = \frac{-\rho_t I}{2\pi^2 r_0^2}\int_0^{2\pi/\hat{z}}\sin(n\hat{z})\sum_{k=0}^{\infty}[D_t(n+2k\pi/\hat{z}) \times (n+2k\pi/\hat{z})K_0(n\hat{r}+2k\pi\hat{r}/\hat{z})]\,dn. \tag{A21}$$

The interval is divided in four sections $[0,\pi/2\hat{z}]$, $[\pi/2\hat{z},\pi/\hat{z}]$, $[\pi/\hat{z},3\pi/2\hat{z}]$, $[3\pi/2\hat{z},2\pi/\hat{z}]$, and these parts are numerically integrated by the Gaussian quadrature using abscissas and weight factors given by Abramowitz & Stegun (1965). A finer subdivision becomes necessary if the ratio $\hat{r}/\hat{z}$ becomes too large. It can be shown that for $i>0$

$$\lim_{m\to\infty}[D_t(m)K_i(m\hat{r})m] = 0, \tag{A22}$$

so that only a finite summation has to be performed.